UNIVERSITY OF TWENTE.

Faculty of Electrical Engineering, Mathematics & Computer Science

The Perdigão Field Campaign: Evaluation of the Cell Perturbation Method in Atmospheric Simulations

Leendert van Veen

April 11, 2018

Graduation committee:

Chairman: Prof. dr. ir. B.J. Geurts
Multiscale Modeling and Simulation
Applied Mathematics
University of Twente

Supervisor: Prof dr. ir. F.K. Chow
Environmental Fluid Mechanics and Hydrology
Civil and Environmental Engineering
University of California, Berkeley

Independent member: Dr. H.G.E Meijer
Applied Analysis and Mathematical Physics
Applied Mathematics
University of Twente

Abstract

State-of-the-art modeling methods are used to simulate the flow over highly complex terrain as documented during the 2017 Perdigão Field Campaign (Portugal). A one-way nesting technique in the Weather Research and Forecasting (WRF) model distinguishing four levels is used to capture the broad range of scales of motion. A new coupling strategy, the Cell Perturbation Method (CPM), is adopted and evaluated using the field data of the campaign. To what extent CPM is contributing to the numerical predictions is the main question addressed in this research. Different model configurations are compared and both qualitative and quantitative comparisons are evaluated to demonstrate the contributions of CPM to the overall results. The domain definition is found important and the robustness of CPM is shown by field comparisons. Wind direction comparisons with tower data of eight different towers show a better agreement for towers measuring the mean flow. Wind speed is under-predicted for all the towers and only the average magnitude of the prediction of turbulent kinetic energy (TKE) has a reasonable agreement with some of the tower data. Comparison with a simulations without CPM shows that the inclusion of CPM does not alter the simulated results significantly.

Contents

1 Introduction

Mesoscale to microscale modeling can be used to efficiently represent the broad range of scales of motion in atmospheric flows. Mesoscale modeling is typically done with resolutions of $O(1 - 10\ \mathrm{km})$, while microscale modeling uses a much finer resolution, $O(1 - 10\ \mathrm{m})$. At the largest mesoscale grids, turbulence is only represented in an average sense, while at finer scales the resolution is fine enough to resolve some of the energy-containing eddies. Using grid nesting, the comparably smooth solution from the mesoscale grid can be interpolated to a nested, much finer grid to represent lateral boundary conditions for the Large Eddy Simulation (LES). As a consequence, the lateral boundary conditions imposed on the nested LES domain do not contain the energy scales required to match the three-dimensional eddies which can be resolved on the LES domain.

Recent work has developed a technique to computationally 'enhance' the mesoscale solution imposed at the LES boundaries which needs to improve the coupling between the nested models. Small scale energy is introduced with the aim of significantly speeding up the numerical transition from the rather smooth solution imposed at the boundaries of the LES domains. These leads to a much more energetic representation of the finer scales which are resolvable in the nested LES domain. This has the virtue of reducing computational costs, since nested LES domain does not have to be enlarged to represent the same energetic representation of the finer scales. In this research we exploit the recent 2017 Perdigão Field Campaign data to support a first validation of the so-called cell perturbation method (CPM), as pioneered by Muñoz-Esparza et al. [2014], when applied to flow over highly complex terrain. To what extent CPM contributes to the quality of numerical predictions is the main question addressed in this report.

Generating the appropriate turbulent length scales at inflow boundaries has been a long-standing challenge in numerical simulations. Various strategies have been proposed with applications ranging from hybrid RANS-LES models in aerodynamics modeling [Lardeau et al., 2007] to multiple level nested modeling in atmospheric boundary layer modeling [Mirocha et al., 2014]. A well known method is the so-called recycling method [Lund et al., 1998]. This method computes the solution of the flow at a vertical plane located in the LES domain parallel to the inflow boundary and uses this solution as lateral boundary condition for the domain of interest at each time step. This way the flow at the inlet of the domain is fully developed. However, due to the recycling technique of the flow solution, periodicity may influence the flow solution. In case of a nested atmospheric flow model with variable inflow and outflow conditions along each boundary, measurement data can be used to generate consistent boundary conditions. Nakayama et al. [2012] used a recycling strategy to generate turbulence for a boundary-layer flow over urban areas. The fluctuating components at a downstream station were added to the mean winds at the inflow. This method showed promising results. However, the method is hard to implement when the dominant wind-direction changes in time.

As an easy-to-implement method, Mirocha et al. [2014] examined the addition of sinusoidal perturbations in both horizontal directions to the potential temperature and velocity fields on the nested LES domain near the inflow boundaries. The added perturbations accelerated the formation of turbulent structures in simulations of neutral atmospheric conditions. In this method it is a challenge to define the different parameters of the perturbations, e.g., magnitude, timescale and location of the perturbations. Muñoz-Esparza et al. [2014] tested different methods based on direct perturbation of the potential temperature field. They found their cell perturbation method (CPM) to be the simplest and most efficient in accelerating the generation of small-scale dynamic content in the numerical turbulence. This method superimposes pseudo-random perturbations to the solution at grid points near the inflow boundary. In fact, the same perturbation magnitude is added to patches of 8×8 grid points (cells). Muñoz-Esparza et al. [2015] applied CPM over flat terrain in combination with a broad range of atmospheric large-scale forcings. Important parameters were identified and suitable values were advised for various atmospheric conditions.

CPM was initially developed for numerically accelerating the transition between a smooth mesoscale solution and a full three-dimensional turbulent flow. Recently, different papers have highlighted the advantage of using such a perturbation method also when the solution from the parent domain contains (under-resolved) turbulence. Mirocha et al. [2014] found that adding perturbations on lateral boundaries of a fine LES domain nested within a coarse LES domain significantly accelerated the development of turbulence. In this approach, small scales were added to inertial range eddies advecting in from the parent domain. Mazzaro et al. [2017] showed that the cell perturbation method can be beneficial when the solution on the parent mesoscale domain contains under-resolved convection. The under-resolved convective structures may be broken down to smaller structures by the perturbation method, thereby explicitly adding to the dynamic content of the solution. Propagating such numerically added small-scale structures with a Navier-Stokes solver may rapidly yield good approximations of the actual turbulent flow even quite close, downstream of the perturbed cells.

These previous studies were performed for idealized setups [Muñoz-Esparza et al., 2015] and over relatively flat domain [Muñoz-Esparza et al., 2017, Jähn et al., 2016]. Muñoz-Esparza et al. [2017] used CPM to successfully reduce the computational cost of a diurnal cycle simulation. It was found that the so-called fetch, i.e., the distance from the domain boundary needed to develop appropriate turbulence length scales, could be significantly reduced in the highest-resolution LES domain when perturbations were applied. CPM was applied to the LES domain, nested within a parent mesoscale domain. For stably-stratified conditions, this approach was also successfully applied to a second LES domain nested within a coarser LES domain. Without the CPM, neither of the LES domains developed turbulence, pointing at a baseline simulation with resolution and numerical dissipation issues. In this case the inclusion of CPM led to qualitative improvements of the numerical solution, toward a genuinely turbulent flow.

The question whether CPM is beneficial in simulations over a real domain with complex topography has not yet been addressed in literature. The generation of small-scale turbulence on the nested domain is accelerated by the presence of finer length scales linked to the specific topography in the domain. On the other hand, this may not be sufficient for the appropriate turbulent length scales to develop in the domain with a reasonable fetch. In this research we implement CPM in WRF in which we closely follow the setup of Muñoz-Esparza et al. [2015]. To quantify the performance of CPM, the simulated results will be compared to field data from the Perdigão campaign. This site consists of two (almost) parallel ridges surrounded by rolling hills. Moreover, the field site has been equipped with various measurement equipment which resulted in an unprecedented amount of available data, ready to exploit in a detailed validation.

The organization of this report is as follows. A description of the Perdigão dataset which we used to validate the computational model is given in Section 2. The numerical setup including CPM settings that are used for these simulations can be found in Section 3. The results of simulations and how these compare to field data can be found in Section 4. Finally, the main findings and conclusions are summarized in Section 5.

2 Dataset: Perdigão Field Campaign

2.1 General Background

The Perdigão Field Campaign was part of the New European Wind Atlas (NEWA) project, a mega-project funded by the European Union. As part of this project, the Perdigão Field Campaign focused on collecting data of mean flow and turbulent wind fields over a complex terrain site with two parallel ridges and a single wind turbine on top of the southwest ridge. The main focus was on better understanding the dynamics of the flow induced by complex terrain and to improve numerical models to better represent the physics of the flow over such terrain.

The Perdigão site is shown in Figure 2.

One of the goals of the Perdigão study is to improve representation of turbulence for LES of flow over complex terrain. Previous studies of flow over Askervein Hill [Chow and Street, 2009] showed that significant numerical errors arise due to the choice of turbulence closure and land-surface representation. The Perdigão site includes steeper and more complex terrain compared to the Askervein Hill case which has been used as a recent benchmark for modeling flow over complex terrain.

The Perdigão site features a valley, Vale do Cobrão, located near the village of Perdigão. The valley is enclosed by two (almost) parallel ridges with a length of 4 km and about 1.4 km apart. The wind direction is often perpendicular to these ridges (Fig. 1), from both sides, which makes the site very interesting for detailed cross-valley flow studies. Using the dense instrumentation of the site, better insight into the magnitude of numerical errors may be achieved.

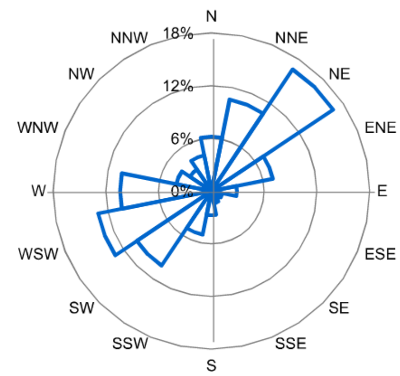

Figure 1: Wind rose for the Perdigão site for a whole year. Wind is often perpendicular to the ridges.

The evening transition between day and night of May 9, observed between $1900-1930$ local time (LT), or $1800-1830$ UCT, is selected to study the use of CPM within the Perdigão case study. This date showed fairly strong south-easterly winds nearly perpendicular to the ridges and additionally the weakly convective conditions are well-suited for studying the influence of CPM. The height up to which the perturbations are applied is dependent on the height of the planetary boundary layer (PBL), which increases for convective conditions and decreases for stable, nighttime condition. Moreover, the generated perturbations are suppressed in stably stratified conditions at night and persist during the weakly convective evening transition.

2.2 Measurement Equipment

The field site was deployed with state-of-the-art instrumentation to capture high resolution flow characteristics. A total of 48 towers, varying in range from 10 to 100 m, were located in and around the valley. The locations of these towers can be found in Figure 2.

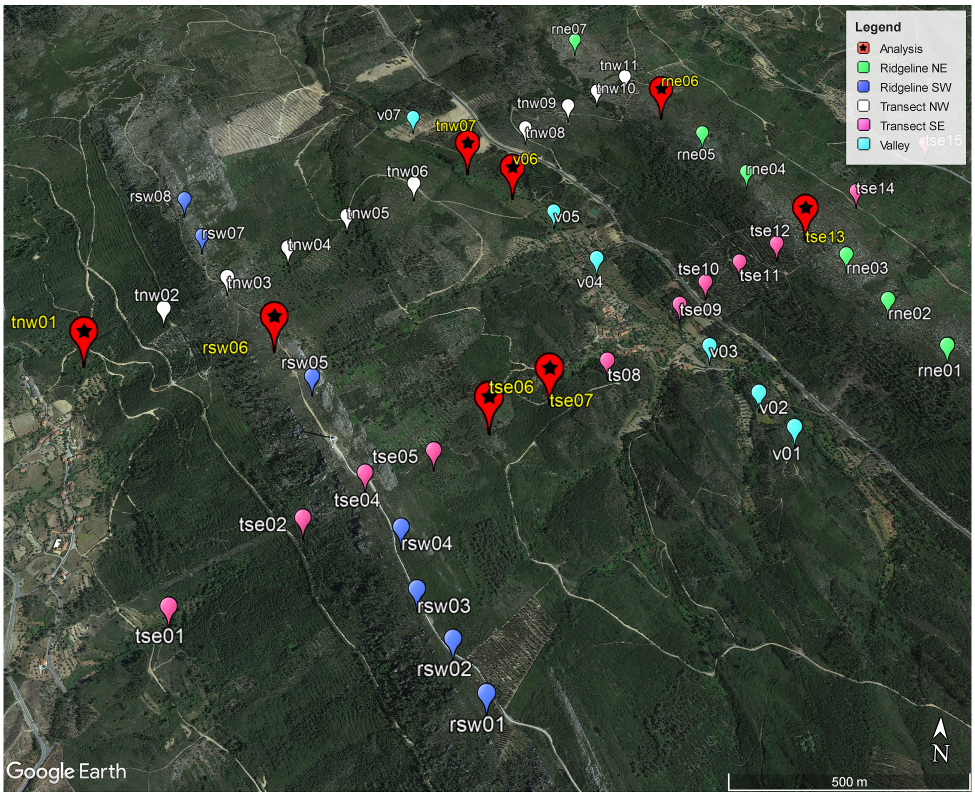

Figure 2: Location of the towers at the Perdigão field site with the towers labeled into four different groups. The red, star icons indicate the locations of the towers used in this research. Screenshot from Google Earth.

The layout of the towers was chosen to characterize the major features of the flow. As shown in Figure 2, two groups of towers were located on top of the ridges, labeled ’rne’ and ’rsw’ for the NE ridgeline and SW ridgeline, respectively. A third and fourth group of towers were located on two different transects of the valley, labeled ’tnw’ and ’tse’ for the transect at the north-west and south-east side of the valley, respectively. A fifth group of towers was located in the valley, aligned with the ridgelines, labeled 'v'. Unfortunately, not all the measurement equipment successfully measured the needed variables. Therefor eight different towers were chosen for the analysis, namely *rsw06*, *rne06*, *tse13*, *tnw01*, *tnw07*, *v06*, *tse06* and *tse07*. These towers represented the top of both the ridgelines (*rsw06*, *rne06* and *tse13*), the valley (*v06*, *tnw07*, *tse06* and *tse07*) and the upstream conditions (*tnw01*). The measurements for all towers were at 20 m above ground level (AGL), except for *tse13* at 100 m AGL and *tse06* at 60 m AGL. By choosing these tower locations a comparison at fixed height AGL between ridges, upstream location and the valley is possible. Moreover, the measurements at the tower locations of *tse13* at the NE ridgeline and *tse06* in the valley can be used to compare the results higher aloft.

The towers were equipped with three dimensional sonic anemometers from which the three dimensional wind speeds u_i, as well as the Reynolds stresses $\overline{u_i'u_j'}$ were obtained. The available tower data had a five minute time interval. The turbulent kinetic energy (TKE) of the flow can be computed using the Reynolds stresses, as will be explained in Subsection 4.3.

3 Numerical Setup

3.1 WRF Numerical Scheme

Multiscale simulations of the evening transition of May 9 were performed using the Weather Research and Forecasting (WRF) model, version 3.9.1.1 [Skamarock and Klemp, 2008]. WRF is equipped with a third-order Runge-Kutta time integration scheme and an Arakawa C-grid staggering for spatial discretization (see figure 3).

The vertical coordinate η is terrain-following and is given by (1),

$$\eta = \frac{p_h - p_{ht}}{p_{hs} - p_{ht}}. \tag{1}$$

with p_{hs} defined as the hydrostatic pressure at the surface of the Earth, p_{ht} the hydrostatic pressure at the top of the air column and with p_h the pressure at a height h, linked directly to

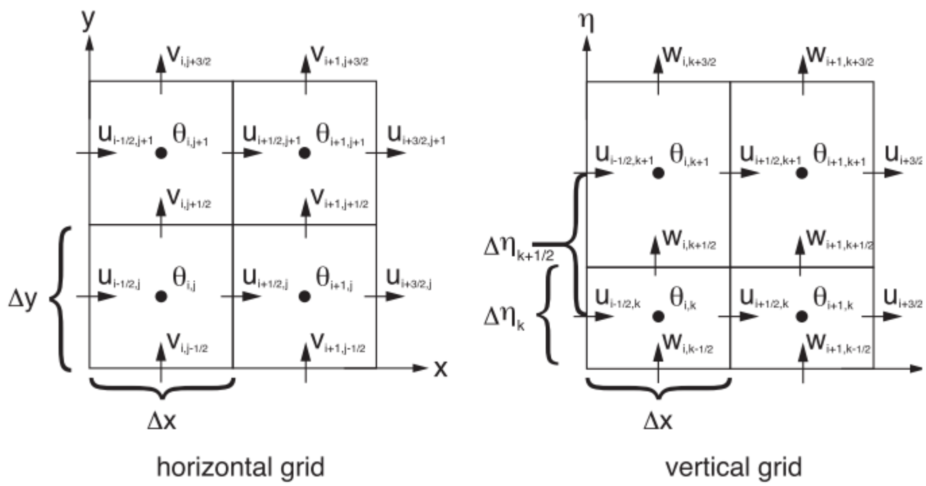

Figure 3: Arakawa grid staggering with potential temperature θ, three dimensional velocity components u, v and w and spatial coordinates x, y and η (from Skamarock and Klemp [2008]).

η. Each η-level has equal hydrostatic pressure, where $\eta = 0$ equals the top of the domain and $\eta = 1$ describes the Earth's surface of the domain (see Figure 4). The simulations here define the domain top as $p_{ht} = 100$ hPa, which coincides with an altitude of approximately 15 km.

Aligning the η-levels with the terrain simplifies the application of the lower boundary conditions. However, the terrain-following coordinates can cause errors in simulations over complex terrain due to the high aspect ratio of the computational cells, especially when the vertical grid spacing is decreased near the ground [Daniels et al., 2016]. An increase in the vertical resolution requires a corresponding increase of the horizontal resolution to keep the aspect ratios and skewness of the grid cells near the boundary within reasonable limits. This clearly has its repercussions for the temporal resolution, which needs to be reduced considerably as

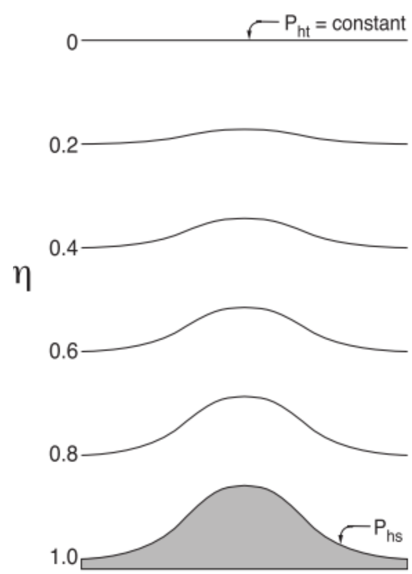

Figure 4: Vertical discretization by terrain following η-levels (from WRF User Guide).

well to adhere to a CFL condition and hence maintain stability of the explicit time-stepping method. Avoiding large aspect ratios and skewness of the grid cells when increasing the vertical resolution is the main reason that simulations over complex terrain need to employ very small time steps. This makes simulations over complex terrain particularly expensive compared to those over flat terrain.

3.2 Multiscale Modeling Strategy

To efficiently represent the broad range of motions, a 4-domain nested setup is used, identifying $D04 \subset D03 \subset D02 \subset D01$. The simulation thus includes motions from synoptic scales of the order of 1000 km, all the way down to turbulent eddies in the lowest part of the atmosphere where resolutions as fine as a few meters may be achieved. The four domains are shown in figure 5 and the sizes of the domains are given in Table 1.

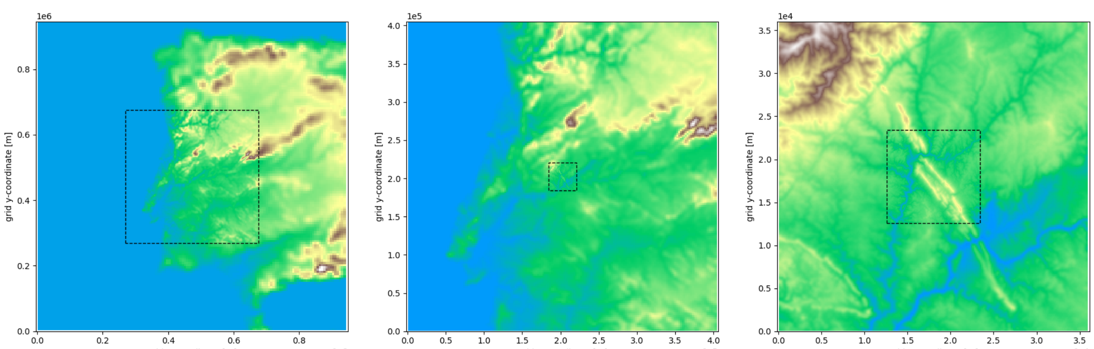

(a) Domain 1 and 2. (b) Domain 2 and 3. (c) Domain 3 and 4.

Figure 5: Four domain nesting setup. Squares indicated by the dashed lines show the spatial extent of the next nested domain.

The different domains in the nested approach utilize different turbulence closure schemes. Domains with a rather coarse resolution ($\Delta x \geq 1000$ m) are equipped with a mesoscale turbulence closure. Since the resolution of these grids is too coarse to actually resolve any turbulent motions, all the subgrid-scale processes are estimated by the mesoscale model. The coarsest domains D01 and D02 are equipped with the Mellor-Yamada Nakanishi and Niino (MYNN) Level 2.5 turbulence closure scheme [Nakanishi and Niino, 2004]. The choice of the MYNN model was made following the sensitivity analysis carried out by Muñoz-Esparza et al. [2017]. Under convective conditions, the dominant turbulence scales are of the order of 100 m so these can be partially resolved in D03 and D04 and subfilter-scale turbulence can be represented with an LES closure model. In this study we employ the 1.5-order TKE closure scheme [Lilly, 1967]. All computational dimensions are listed in Table 1.

Table 1: Physical and computational dimensions of the nested grids, with n_x, n_y and n_z the number of grid points in each dimension, Δx and Δy the horizontal grid resolutions, Δz_{min} the vertical grid spacing of the first grid point, L_x (km) and L_y (km) the horizontal domain sizes and Δt the temporal resolution.

	n_x	n_y	n_z	Δx (m)	Δy (m)	Δz_{min} (m)	L_x (km)	L_y (km)	Δt (s)
D01	141	141	59	6750	6750	60	945	945	30
D02	181	181	59	2250	2250	60	405	405	10
D03	241	241	71	150	150	30	27	27	0.5
D04	361	361	117	30	30	15	10.8	10.8	0.05

The resolutions of the grids on the two outermost domains D01 and D02 are $\Delta x = 6.75, 2.25$ km, respectively and the resolutions of the grids on the two innermost domains D03 and D04 are $\Delta x = 150,\ 30$ m. All the grids are uniform in x and y direction in the horizontal plane. On these grids it is possible to capture the large-scale dynamics including that induced by the ocean on D01 and D02, as well as some of the turbulent eddies on D03 and D04. In addition, the domain D04 was made big enough to capture the entire valley, including the ridges. The choice of domain size of D03 is explained in Subsection 4.2. The simulations were forced in D01 by analysis data from 0.25 by 0.25 degree global latitude and longitude grid from the Global Forecasting System (GFS), which is about 27.8 km by 21.4 km in the specific case of the Perdigão field site. GFS is a global weather prediction model which is initialized four times a day by the National Weather Service of the United States and has an 3-hourly output, consisting of both analysis (which incorporate observation data) and predicted fields. GFS data from each interval is interpolated to provide lower and lateral boundaries for D01 as well as initial conditions for the simulations. The two outermost mesoscale domains, D01 and D02, are initialized on May 9, 0600 LT, D03 is initialized at 1200 LT, and D04 is initialized at 1500 LT. All the domains are run until 1930 LT. The analysis focuses on the prediction of flow characteristics between 1900 LT and 1930 LT ($1800 - 1830$ UTC), when the influence of CPM is most noticeable.

The nesting ratio between the domains D02 and D03 ($\Delta x_{D02}/\Delta x_{D03} = 11$) is bigger than the commonly used value of 3 to 5. The reason for this large nesting ratio is because both mesoscale and LES closure schemes have difficulty when the resolution of the domain is in the so-called Terra Incognita (TI) regime [Wyngaard, 2004, Zhou and Chow, 2014, Zhou et al., 2014]. Resolutions in this regime are close to the scale of thermal plumes in the boundary layer which extend to the boundary layer height of order $O(10^3 \text{ m})$. Some of the convective cells or rolls will be resolved at $O(10^3 \text{ m})$ resolution, rather than requiring parameterization through the turbulence model. This is in contrast to the assumption in mesoscale models that the turbulence scheme captures all the turbulence and that no turbulent motions are resolved. On the other hand, LES models running with TI resolutions also fail to accurately represent the flow because the resolution is not fine enough to resolve all the energetic eddies. Simulation results at TI resolutions can affect finer nested simulations by passing in erroneous information about resolved structures [Zhou and Chow, 2014]. By adopting a large nesting ratio of 11 we largely 'skip' the TI regime and attempt to by-pass these complications. We do, however, put significant emphasis on the generation of appropriate scales using this nesting strategy, which is the focus of the CPM study here.

The vertical grid nesting capability [Daniels et al., 2016] implemented in WRF version 3.7 and improved in WRF version 3.8 is used here to adjust vertical resolution on each of D01-D04. As clarified by Daniels et al. [2016], near-surface vertical resolutions of the order of a few meters imply computational cells with very high aspect ratios when combined with a coarse horizontal grid. These high aspect ratios cause additional numerical errors over complex terrain due to the use of terrain following coordinates, as explained in Subsection 3.1. We use a vertical resolution near the ground on the innermost LES domain D04 of 15 m and on the two outermost domains D01 and D02 of 60 m. Choosing a finer vertical resolution on D04 led the simulation to blow up. The grid spacing of the domains was increased higher aloft up to 450 m for D01-D03 and 250 m for D04 at the top of the domain, which was placed at $p_{ht} = 100$ hPa. The discretization of the first 2000 m on each domain is shown in Figure 6.

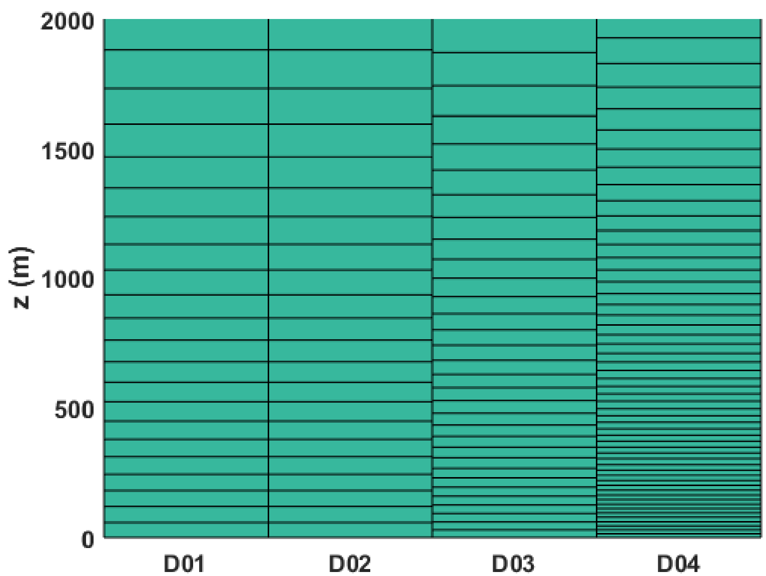

Figure 6: Vertical discretization of the four domains. Only the first 2000 m above ground level is shown.

3.3 Cell Perturbation Method

The cell perturbation method was developed by Muñoz-Esparza et al. [2014] and improved in Muñoz-Esparza et al. [2015]. The method is based on perturbations of the potential temperature, used in Mirocha et al. [2014]. The idea is to perturb the potential temperature values on patches of grid points near the inflow boundaries of the LES domain. These patches are referred to as 'cells'. Which of the boundaries are inflow boundaries at a given moment is determined by re-computing the average wind direction over each boundary. The perturbations are renewed periodically after a so-called 'perturbation time' t_p. Moreover, the random amplitude of the perturbations in each cell is distributed uniformly over an interval $[-\tilde{\theta}_{pm}, +\tilde{\theta}_{pm}]$. Here, $\tilde{\theta}_{pm}$ is the maximum perturbation magnitude, determined dynamically during the simulations. The value of $\tilde{\theta}_{pm}$, as well as the value of t_p, is made dependent on the flow speed in a manner specified below. The method has very low computational costs and is easy to implement.

In our setup we used horizontal cells consisting of 8×8 grid points. The motivation for using eight grid points is that the numerical diffusion of the WRF model dissipates energy rapidly for $k \geq 2\pi/(7\Delta x)$ [Skamarock, 2004]. Therefore, any perturbation imposed with a shorter wavelength than $8\Delta x$ does not contribute much to the development of turbulence. These patches are located near the inflow boundaries of the nested LES domain; three rows of patches parallel to the boundary are imposed, covering the first 24 grid points downstream into the domain. We followed Muñoz-Esparza et al. [2015] in this setup. Figure 7 shows the potential temperature field on the inner part of D02 (the outer domain with coarser grid cells) and D03. The three rows of patches near the south and east boundaries of D03 are visible, displaying an intermediate coarseness between the resolution of D02 and the resolution used inside D03.

The two yet-unknown parameters in this method are the maximum perturbation magnitude $\tilde{\theta}_{pm}$ and the perturbation time period t_p. Following Muñoz-Esparza et al. [2015], we identify two non-dimensional numbers from which these parameters can be computed: the perturbation Eckert number $Ec = U_g^2/c_p\tilde{\theta}_{pm}$ and the perturbation time-scale $\Gamma = t_p U_w/d_c$. Here, U_g is the geostrophic wind speed, c_p the specific heat capacity at constant pressure, U_w a measure for the so-called 'weakest' wind speed in the domain, and d_c the length of the path across the perturbed

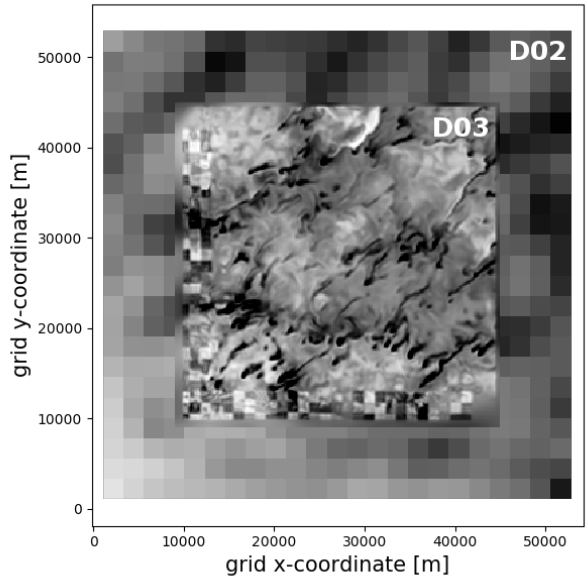

Figure 7: Potential temperature field on D03 showing detailed structures, nested in D02, showing coarser spatial resolution. The application of CPM is easily recognized by the intermediate coarsening in 8×8 grid points at the west and south boundaries, which turned out to be the inflow boundaries at this particular instance.

cells, when traversing the cells in the direction of the local mean wind. All these four values can be obtained during the simulations, such that t_p and $\tilde{\theta}_{pm}$ can be computed dynamically upon selecting suitable values for Ec and Γ.

The perturbation Eckert number expresses the interaction between the geostrophic forcing and the buoyancy contribution induced by the potential temperature perturbations. CPM was tested for different geostrophic forcings by Muñoz-Esparza et al. [2015] who advised an optimal Eckert number of $Ec = 0.2$. This value is also used in our simulations. If the Eckert number is set too low, the perturbations are dominated by buoyancy effects and exaggerate the distortion of the velocity field near the inflow boundaries. Moreover, the resulting strong perturbations due to a high $\tilde{\theta}_{pm}$ result in rather unphysical separated high- and low-speed areas. On the other had, if the Eckert number is set too high, the effect of the imposed small-amplitude perturbations is hardly noticeable as the maximum amplitude is correspondingly small.

The perturbation time scale Γ is found by Muñoz-Esparza et al. [2015] at $\Gamma = 1$. The time scale describes the time that it takes to cross a cell at the 'weakest wind' velocity. A perturbation time-scale lower than 1, i.e., a short perturbation time t_p, results in an amplification of the instabilities. On the other hand, setting $\Gamma \leq 1$ results in an alternating laminar and turbulent flow. As recommended by Muñoz-Esparza et al. [2015], $\Gamma = 1$ is used. The distance across the perturbed cells d_c used in Γ is computed as $d_c = 1/\cos(\hat{\phi}) \cdot 24\Delta x$ where $\hat{\phi}$ is the average wind direction over every grid point at the inflow boundaries and the number 24 originates from three rows of 8 grid cells.

To compute the weakest and geostrophic wind speeds, the settings of Muñoz-Esparza et al. [2015] were adopted, namely setting the geostrophic wind speed U_g as the horizontal wind speed at the boundary layer height z_i and the weakest wind speed U_w as the horizontal wind speed at the first grid point above the Earth's surface, U_1. Moreover, the perturbations were applied up to $2/3z_i$, as was recommended by Muñoz-Esparza et al. [2014] to avoid interference of the perturbations with the inversion layer, which could potentially trigger numerical instabilities. However, following this original proposal, the perturbations did not accelerate the generation of turbulence significantly. Therefore, a few adjustments were made.

Due to the very shallow boundary layer during the evening transition, the factor of $2/3$ was increased up to 0.9, to make the perturbed region in the vertical direction larger in an attempt to trigger turbulence also higher aloft. We did not encounter any numerical instabilities in this new setup. To make sure that the perturbations were strong enough, the geostrophic wind speed was evaluated at $1.1z_i$ instead of at z_i. Finally, since the wind speed at the lower three vertical levels was very low, the horizontal wind speed at the fourth grid-point above the surface was used to evaluate the weakest wind speed $U_w = U_4$. After these adjustments a significant improvement in the acceleration of turbulence was observed. This was used throughout the study. How the choice for U_w affects the simulation outcome and to what end these choices are related to the complex terrain is interesting from a reliability perspective and will be investigated in future research.

4 Assessment of Simulation Results using Perdigão Field Data

4.1 Robustness of the Cell Perturbation Method

In this section we compare simulation results obtained with and without CPM, on small and larger domains. CPM is designed to enrich a flow with small-scale motions only, thus the main large-scale flow features should not be affected significantly by CPM. The goal is for CPM to help develop turbulent flow at appropriate scales inside the domain. Hence, comparing simulations without CPM, but on a larger domain with longer fetch available, with CPM enriched simulations on a smaller domain and shorter fetch should ideally yield good similarity. Both vertical velocity profiles as well as energy spectra are analyzed at vertical grid level $k = 8$ at D03, which coincides with an altitude of $\approx$ 260 m AGL. The simulated date is May 9, $1600 - 1930$ LT.

The velocity profiles in Figure 8 illustrate the robustness of global features of the simulation results obtained for the Perdigão site. As a point of reference, Figure 8(a) shows contours of the vertical velocity over an extended domain that contains D03. CPM was not used in this simulation - it will be referred to as *D03 ref*. The vertical velocity contours on the original D03 without CPM, *D03*, are shown in Figure 8(b) and the simulation results with CPM applied on D03, are shown in Figure 8(c).

The simulated results are very similar in the sense that the mean flow structure, based on the vertical velocity profile, does not change significantly. The reference simulation in Figure 8(a) shows a region of high w-velocity magnitude at and around the location of the valley. The same structures appear in Figure 8(b). Hence, the large fetch in Figure 8(a) does not seem to be required to generate the observed flow structures. Figure 8(c) does, in addition, display

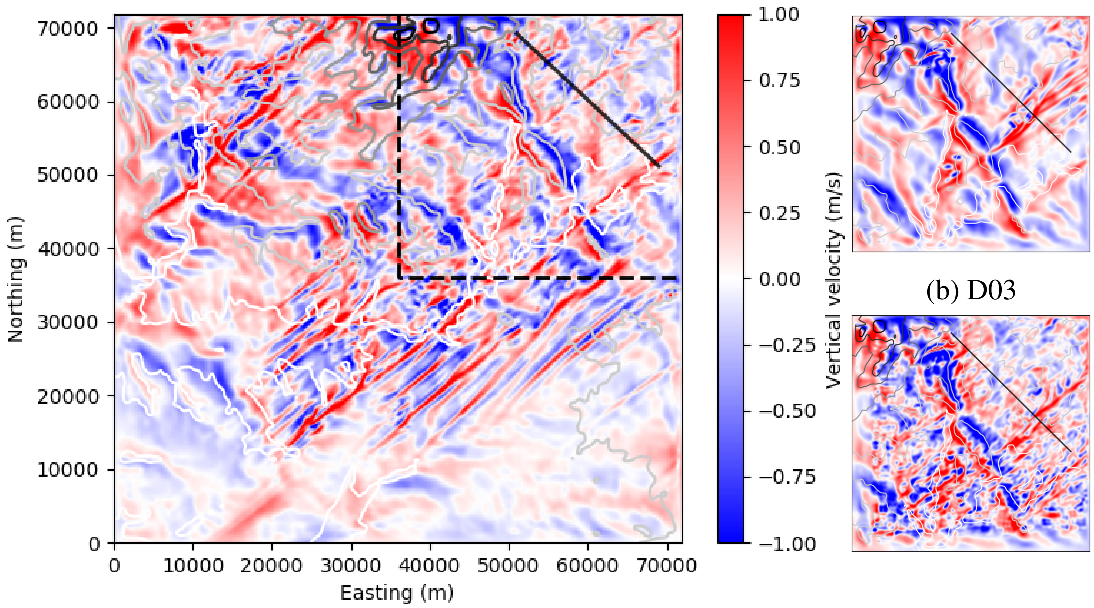

(a) D03 reference

(b) D03

(c) D03 CPM

Figure 8: Vertical velocity profile at 260 m AGL at 1900 LT. Small domain without CPM (b) compared to a large reference domain without CPM (a) and small domain with CPM (c). The dashed lines in (a) show the spatial extent of the original D03. The diagonal line in (a) is used for the shown spectra comparison in Figure 9.

further smaller scale structures induced by CPM. The flow is clearly enriched with small scale motions. Hence, CPM provides an increased control over the degree of small scales that could be exploited to enhance the correspondence with field observations.

To quantify the contributions of CPM to the flow, the energy spectra of the w-velocity over the diagonal line in Figure 8(a) across the domain D03 were computed as well. The diagonal line contains 120 grid points and the spectra are computed following the approach of Durran et al. [2017], averaged over five consecutive time samples with an interval of 150 seconds. The line is located downstream of the valley such that the wind already has crossed the valley and should be fully developed by the time it crosses the diagonal line. The results are shown in Figures 9.

Figure 9 shows that the energy spectra at low wavenumbers ($k \leq 0.003\ \mathrm{m}^{-1}$) are quite

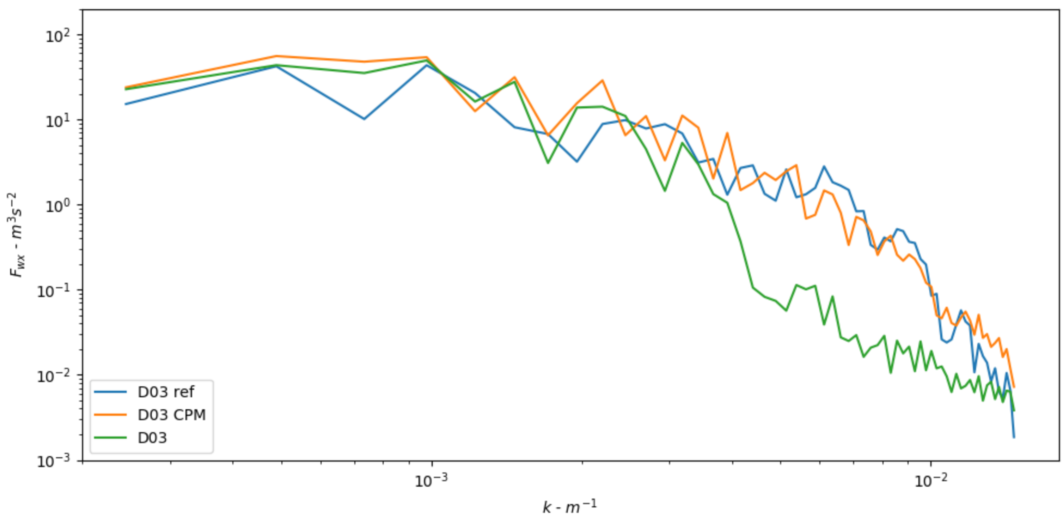

Figure 9: Comparison of energy spectra computed from the w-profile over the diagonal line shown in Figure 8(a). Averaged over five time samples, started at 1900 LT.

similar for all three simulations. However, the energy spectra for higher wavenumbers ($k \geq 0.005\ \mathrm{m}^{-1}$) show significant differences between *D03* and the other two simulations. On the other hand, *D03 CPM* shows a very similar energy spectrum compared to the spectrum of *D03 ref*. This corresponds to the induced wavenumbers by CPM of $k = 2\pi/\left(8\Delta x\right) \approx 0.005\ \mathrm{m}^{-1}$. The increased agreement between results obtained on the small domain with CPM and the reference simulation without CPM on the larger domain, nicely quantify the benefit of CPM concerning the smaller turbulence scales, i.e., similar spectra are obtained with much less fetch. In the next subsection we turn our attention to the influence of the domain definition on the predicted flow.

4.2 Domain Configuration

To systematically compare the influence of different configurations of D03, simulations with three different nested domain configurations are compared. The simulated date is the same as in Subsection 4.1: May 9, $1500 - 1830$ LT. The spatial extent of D03 is kept the same in each of the three simulations, however, the computational grid of the domain is shifted toward the north-east and the south-west. By doing so, we modify the distance from the domain boundary over which the atmospheric flow can evolve within the computation domain before reaching the valley. A shift of the nested D03 of one grid point east and one grid point south on D02 implies a shift of 15 grid points in these directions for D03. Figure 10 shows the locations of the three computational domains for the different setups.

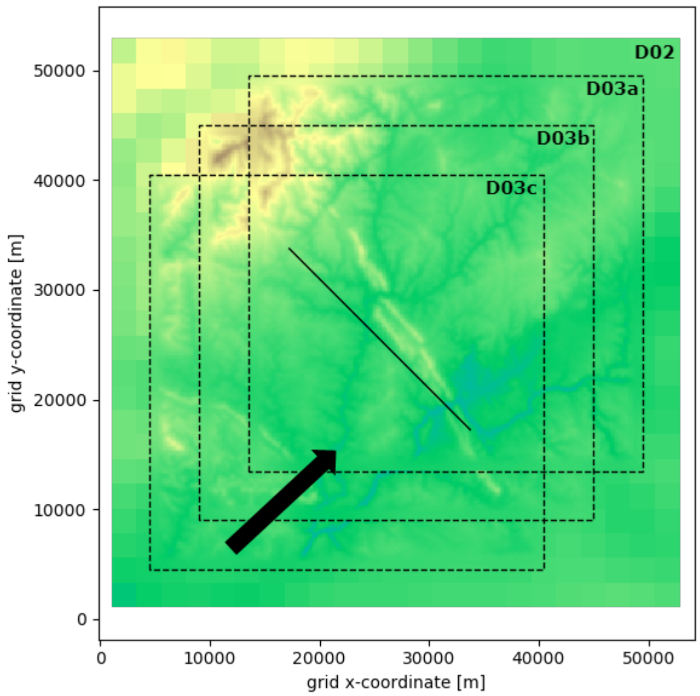

Figure 10: Location of the three different nesting setups of D03 (a-c) within D02. The vertical velocity profiles over the diagonal line are used to compare the energy spectra of the flow for the different domains. The mean flow direction is indicated by the arrow.

D03b is the default computational domain as it is defined in Figure 8(b). D03a is the same computational domain, shifted 30 grid points to the north-east and D03c is obtained by shifting D03b 30 grid points to the south-west. Four simulations are compared: three simulations without CPM on D03 (*D03a*, *D03b* and *D03c*) and one simulations with CPM applied on D03a

(*D03a CPM*). Comparison is done on the basis of energy spectra obtained from the vertical velocity profile at 1900 LT, over the diagonal line shown in Figure 10, similar to the analysis in Subsection 4.1. The computed spectra are shown in Figure 11.

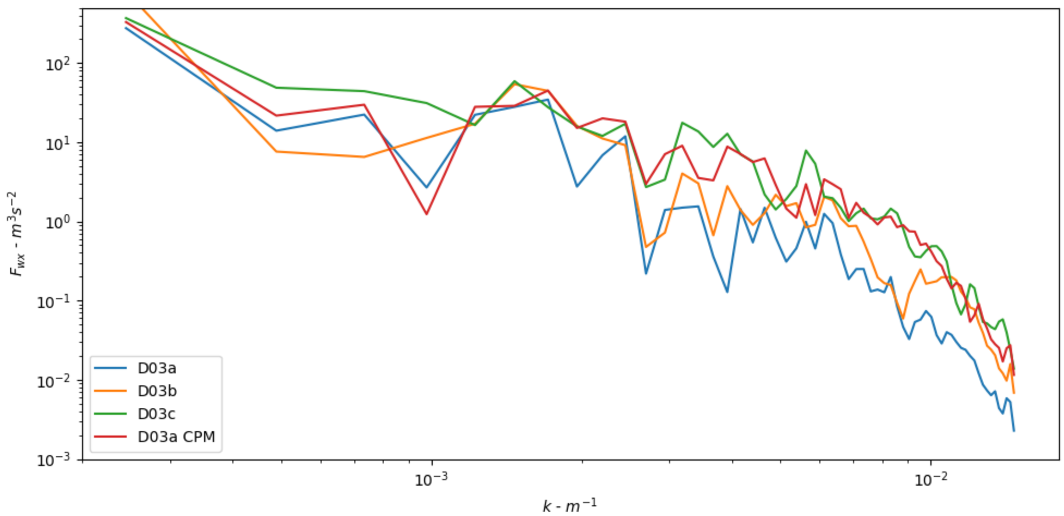

Figure 11: Spectra of the vertical velocity profile over the diagonal line shown in Figure 10, averaged over five time samples, started at 1900 LT. Three simulations without CPM over three domains D03(a-c) and a simulations with CPM over D03a are compared.

The comparison shows a clear difference in energy spectra for the different domain configurations. Spectra extracted from simulations with D03a, i.e., with a shorter distance to the boundary in terms of the prevailing wind direction, are significantly lower. This suggests that the turbulence levels in the flow have not developed as fully as they should in accordance to the flow conditions. Conversely, domains with a larger distance show spectra that represent higher energy levels for higher wavenumbers.

Similar to Figure 9, CPM clearly enriches the energy content of the smaller eddies in the flow. In fact, the simulation with the shortest distance, but with CPM shows an energy spectrum that compares closely with the simulation with the largest distance without CPM. The difference is most obvious for wavenumbers $k \geq 0.005\ \mathrm{m}^{-1}$, which correspond to the wavenumbers added by the perturbations, as explained in Subsection 4.1. This clearly demonstrates the action of CPM toward efficiently generating small-scale turbulence in a compact spatial domain. Application of CPM can therefore be used beneficially to study turbulent flow over complex terrain at reduced costs. Instead of having to increase the size of D03 by about 30 grid points in each direction, one can achieve similar predictions by employing CPM at virtually no computational overhead. In this example, increasing the grid from 241 to 271 nodes in each horizontal directly would be an increase of 26% in computational cost.

In the next subsection the simulated results are compared to field data. The domain configuration of D03b including CPM is used for the simulations to ensure a fully developed flow over the two ridges.

4.3 Comparison to Field Data

In this subsection, the simulated results are compared to field data from the Perdigão field campaign. In contrast to the results shown in the previous two sections, the simulated results in this section are taken from the innermost domain, D04. This domain has the highest spatial resolution and allows for most detailed comparisons with field data. CPM is applied on both D03 and D04 to ensure that the flow is stimulated in its development across the domain. The simulated time is the same as before, $1600 - 1930$ LT, or $1500 - 1830$ UCT.

For comparison with tower data, data from eight different towers are used: *rsw06, rne06, tse13, tnw01, v06, tnw07, tse06* and *tse07*. The locations of the towers can be found in Figure 2, Subsection 2.2. All the tower measurements are taken at 20 m AGL, except for *tse13* at 100 m AGL and *tse06* at 60 m AGL. Three different variables are compared, namely the wind speed U, wind direction ϕ and the turbulent kinetic energy (TKE). The eight towers are chosen in a specific manner to test the computational model over a range of demanding conditions. Two different groups of towers are considered, namely the towers that align well with the simulated wind direction, shown in Figure 12, and towers that do not line up so well, shown in Figure 13.

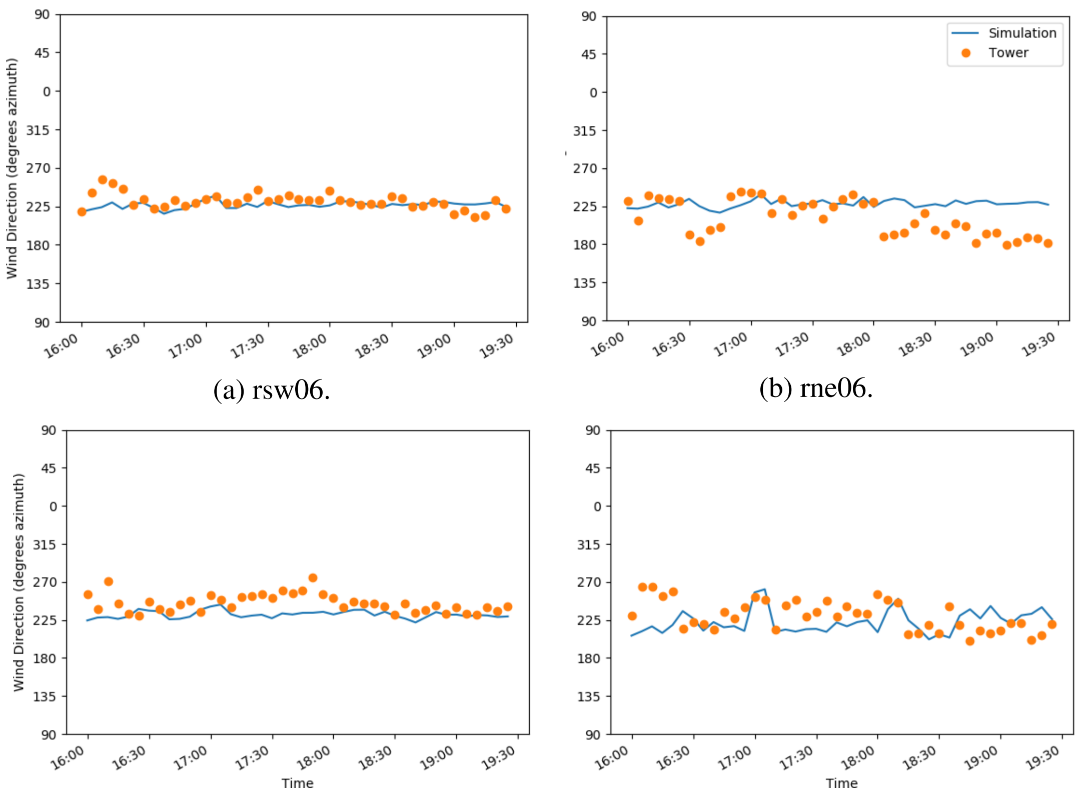

(a) rsw06.

(b) rne06.

(c) tse13.

(d) tnw01.

Figure 12: Wind direction comparison between simulated data and tower measurements taken at a ridgeline. Results in (a), (b) and (d) are measured at 20 m AGL and (c) is measured at 100 m AGL.

The towers *rsw06* and *rne06* are located at the top of the SW and NE ridgelines, respectively. The simulated wind direction at 20 m AGL at the location of these towers in Figure 12(a) and 12(b) show a good agreement with the measurements from the towers over the simulation period. Figure 12(b) shows a less good agreement at the end of the time period, which could be explained by weaker wind speeds during the evening transition. Comparison higher aloft, at 100 m AGL, with tower data from *tse13*, located at the NE ridgeline, shows good agreement throughout the entire time period. In addition to the towers on top of the ridges, the comparison of the measurements of the upstream tower *tnw01*, located south-westerly of the SW ridgeline, at 20 m AGL, also shows good agreement. Both the model prediction as well as the measured results show a consistent southwesterly wind (225 degrees), as is expected from the results on D03 shown in the previous subsections.

In contrast, Figure 13 shows the comparisons of simulations with the tower data for towers located behind the first ridgeline, in the valley. The simulated results show an average wind

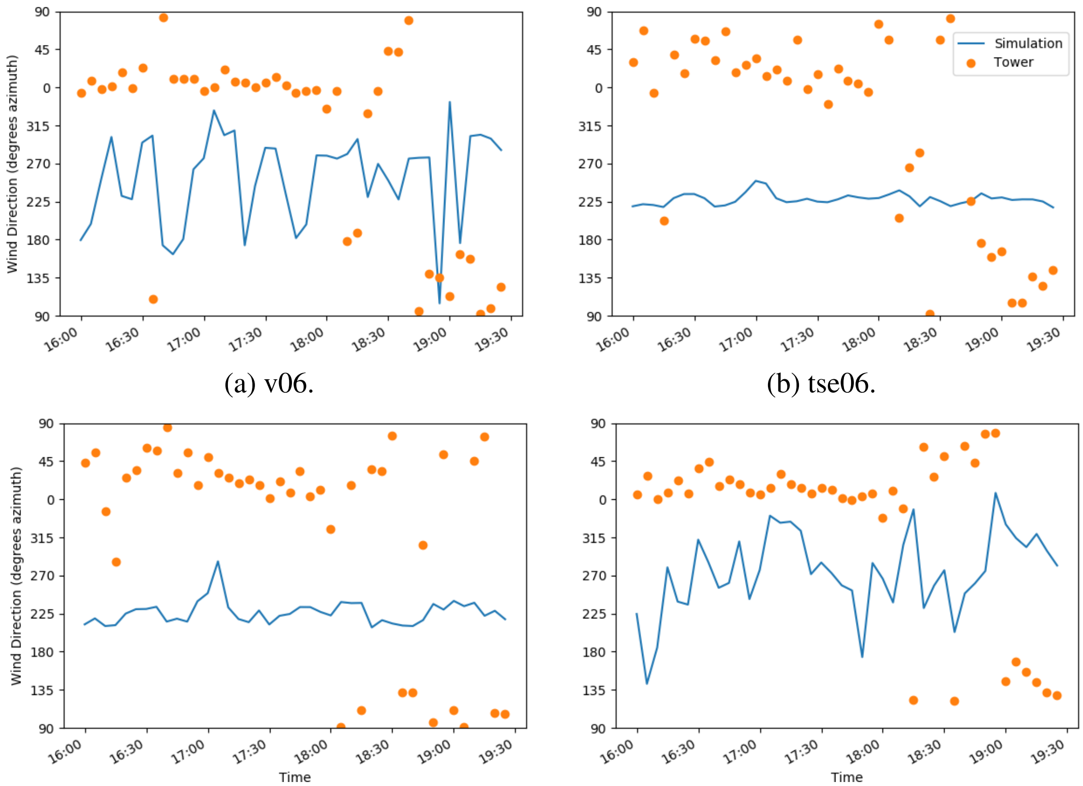

(a) v06. (b) tse06.

(c) tse07. (d) tnw07.

Figure 13: Wind direction comparison between simulated data and tower measurements taken in the valley. Results in (a), (d) and (c) are measured at 20 m AGL and (b) is measured at 60 m AGL.

direction of approximately 250 degrees with considerable variations in some places. The measured data are seen to differ significantly, with an average wind direction of 25 degrees or a north-northwesterly wind until 1800 LT. After 1800 LT, the measured wind direction in the valley shifts rapidly, with very large variations. The large error in the computational approximation of the wind direction can be explained by the influence of the ridges. The flow is possibly getting diverted around the valley and channeled in to the valley from the north, which could explain the northern wind measured by the towers. The model is clearly not capable of simulating this wind shift, not at 20 m AGL (Figures 13(a), (d) and (b)), nor at 60 m AGL (Figure 13(c)).

To further compare the simulated results with tower data, the wind speed comparison for the towers included in Figure 12 is shown in Figure 14. Despite the rather good agreement of

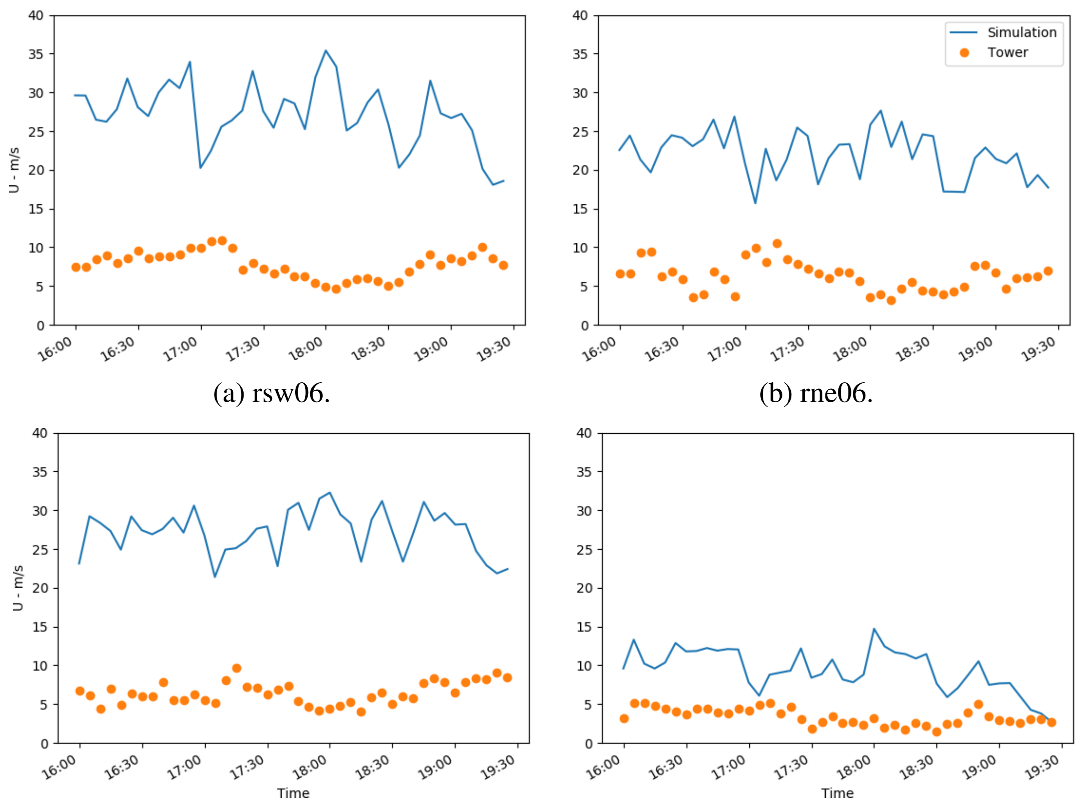

(a) rsw06. (b) rne06.

(c) tse13. (d) tnw01.

Figure 14: Wind speed comparison between simulated data and tower measurements taken at a ridgeline. Results in (a), (b) and (d) are measured at 20 m AGL and (c) is measured at 100 m AGL.

the simulated wind direction and the measured wind direction, the model strongly over-predicts the wind speed at almost all the towers compared. The simulated results at the two ridges at 20 m AGL, shown in Figure 14(a) and Figure 14(b), have an average wind speed of around 25

$\mathrm{m/s}$. However, the measured data shows only a wind speed of around 10 $\mathrm{m/s}$. The same result is shown by the comparison higher aloft, at 100 m AGL, for tower *tse13* in Figure 14(c). The comparison with the tower *tnw01* at 20 m AGL, located upstream from the SW ridgeline, shows a smaller error, but the wind speed is over-predicted for this location as well.

The over-prediction of wind speeds near the surface is a well known problem of WRF [Ngan et al., 2013, Jiménez and Dudhia, 2012]. A possible reason for this over-prediction, given by Jiménez and Dudhia [2012], is the smoother topography used in the model. The unresolved topographic features should produce an additional drag to the already existed drag generated by the parameterized vegetation. An even more plausible reason for the over-prediction is the absence of a canopy model in the simulation, which takes into account the dense vegetation of the valley. Adding a suitable canopy model would increase the drag generated by the vegetation as well.

The wind speed comparisons for towers inside the valley are shown in Figure 15. The results show a better agreement of simulated results with the measurements inside the valley, compared to the towers on top of the ridges. Especially the comparisons of the towers on the north-side of the valley, *v06* and *tnw07*, show a good agreement with the tower data. The very low wind speed also helps interpreting the irregular behaviour in the simulated wind directions in Figures 15(a) and 15(d), because it is well known that the wind direction is more difficult to predict for low wind speeds. The model over-predicts the wind speed for the towers on the south-side of the valley, shown in Figures 15(b) and 15(c). Although all the four towers are located inside the valley, the towers *tse06* and *tse07* are located closest to the SW ridgeline. The over-prediction of the wind speed at the ridgeline could be a possible explanation for the smaller, but still significant over-prediction at the location of the towers *tse06* and *tse07*.

To assess the generated turbulence in D04, the turbulent kinetic energy (TKE) of the simulations is compared with the tower data. The TKE is the kinetic energy per unit mass of the

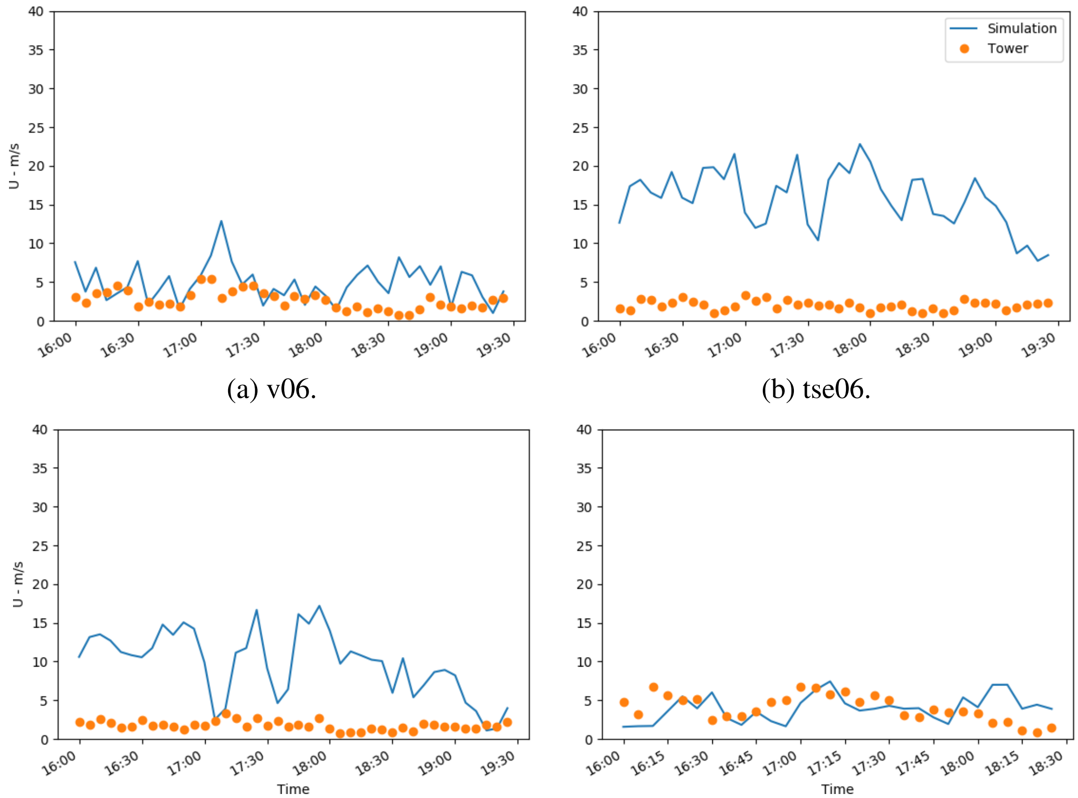

(a) v06.

(b) tse06.

(c) tse07.

(d) tnw07.

Figure 15: Wind speed comparison between simulated data and tower measurements taken in the valley. Results in (a), (d) and (c) are measured at 20 m AGL and (b) is measured at 60 m AGL.

turbulent fluctuations u_i' in a turbulent flow: $TKE = \frac{1}{2}\overline{u_i'u_i'}$. The turbulent fluctuations u_i' were obtained using Reynolds decomposition: $u_i' = u_i - \overline{u_i}$, where $\overline{u_i}$ are the time-averaged velocity components. The Reynolds stress components $\overline{u'u'}$, $\overline{v'v'}$ and $\overline{w'w'}$ as observed in the field data were directly obtained from the tower-data with an interval of 5 minutes. The TKE of the tower measurements was computed with

$$TKE_{towers} = \frac{1}{2}\left(\overline{u'u'} + \overline{v'v'} + \overline{w'w'}\right) \tag{2}$$

To compute the TKE from the simulations, both the resolved TKE and the subgrid-scale TKE were obtained from the model output. The subgrid-scale TKE was modeled by the 1.5-

order TKE closure scheme and hence was available as an output from the simulation. The resolved TKE was computed from the time series U_i from the simulation output. The 5-minute time average $< U_i >$ of the time series was computed, as an approximation of time average velocity components $\overline{u}_i$. Using this average, the fluctuations of the time series were computed: $U_i' = U_i - < U_i >$, after which each entry of the vector U_i' was squared. Finally, the new time series $U_i'U_i'$ was averaged over a time period of 5 minutes for the period of interest ($1600-1930$ LC), similar to the tower data. The resolved TKE is then obtained using the same formula,

$$TKE_{sim,resolved} = \frac{1}{2}\left(\overline{U'U'} + \overline{V'V'} + \overline{W'W'}\right). \quad (3)$$

Due to limited storage capabilities, the output of the simulation on D04 was available at 30 second intervals and accordingly 10 samples were used to average the stress terms $U_i'U_i'$ and obtain the Reynolds stresses $\overline{U_i'U_i'}$. More samples are needed to retrieve an accurate representation of the resolved TKE. However, for the eight towers considered in this section, an average of 93% of the total TKE is contributed by the sub-grid part. Therefor we neglect the error of the resolved TKE in this research.

The TKE comparisons between field data and simulated results for the towers positioned at the ridgeline and upstream are shown in Figure 16. The simulated results for the locations of the towers on the NE ridge, *rne06* and *tse13*, agree much better to the measured data, than for the location of the tower on the SW ridge, *rsw06* and the tower upstream, *tnw01*. The turbulence levels induced by the flow over the valley are much higher for the locations on the NE ridge and are seen to match the simulated results better. The simulated results for the other two towers over-predict the TKE significantly. Moreover, all the tower comparisons show a bad agreement for the temporal behaviour of the TKE budget.

The TKE comparison inside the valley is shown in Figure 17. The average prediction of the TKE magnitude is similar for all four towers inside the valley, i.e., 4.72 ± 0.56 m^2/s^2. In

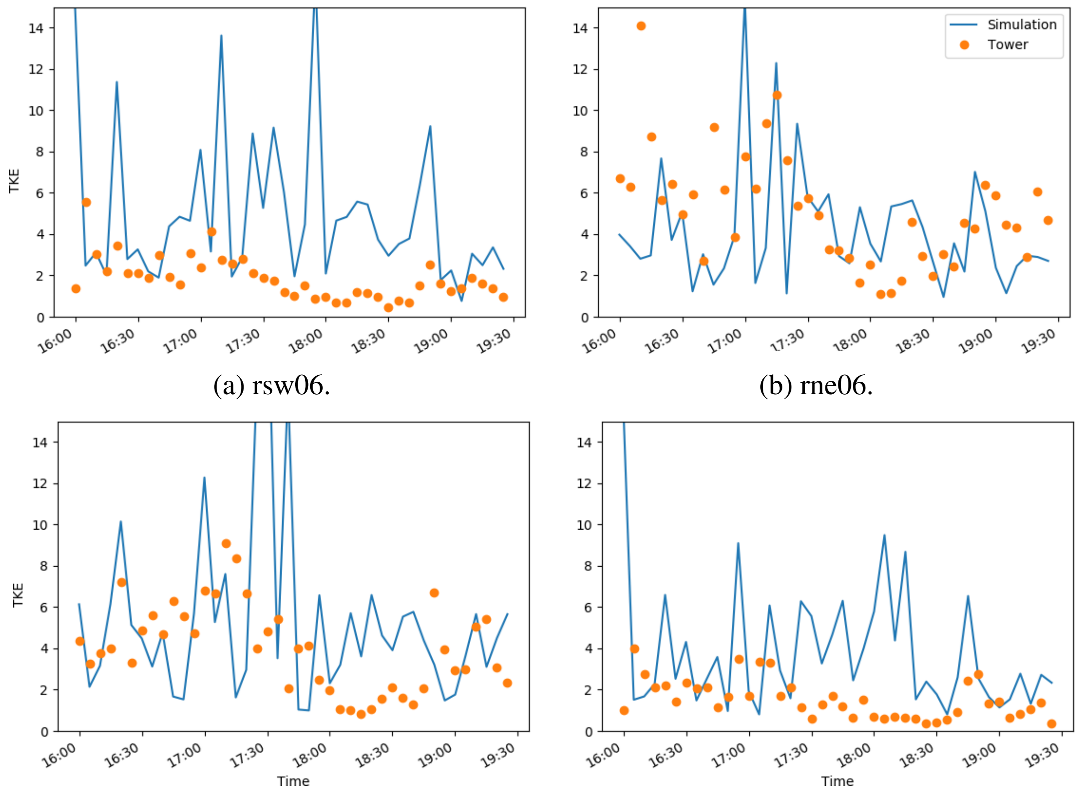

(a) rsw06. (b) rne06.

(c) tse13. (d) tnw01.

Figure 16: TKE comparison between simulated data and tower measurements. Results in (a), (b) and (d) are measured at 20 m AGL and (c) is measured at 100 m AGL.

general, the simulation predicts a higher TKE value with much more temporal variation than is observed at the towers in the valley. There is a significant difference between the predictions and the measurements of the TKE. Apparently, this quantity can not be reliably captured by the model at this resolution, since other papers show a much smaller error, e.g., Rai et al. [2017] and Muñoz-Esparza et al. [2017] show errors $\leq 0.5\ \mathrm{m}^2/\mathrm{s}^s$.

All the results presented in this subsection so far are generated using a model setup with CPM on both LES domains. To quantify the influence of CPM on the accuracy of the simulations, we compare the previous results generated with CPM on both LES domains with results simulated without the use of CPM. As an example, the results for the comparison of the wind

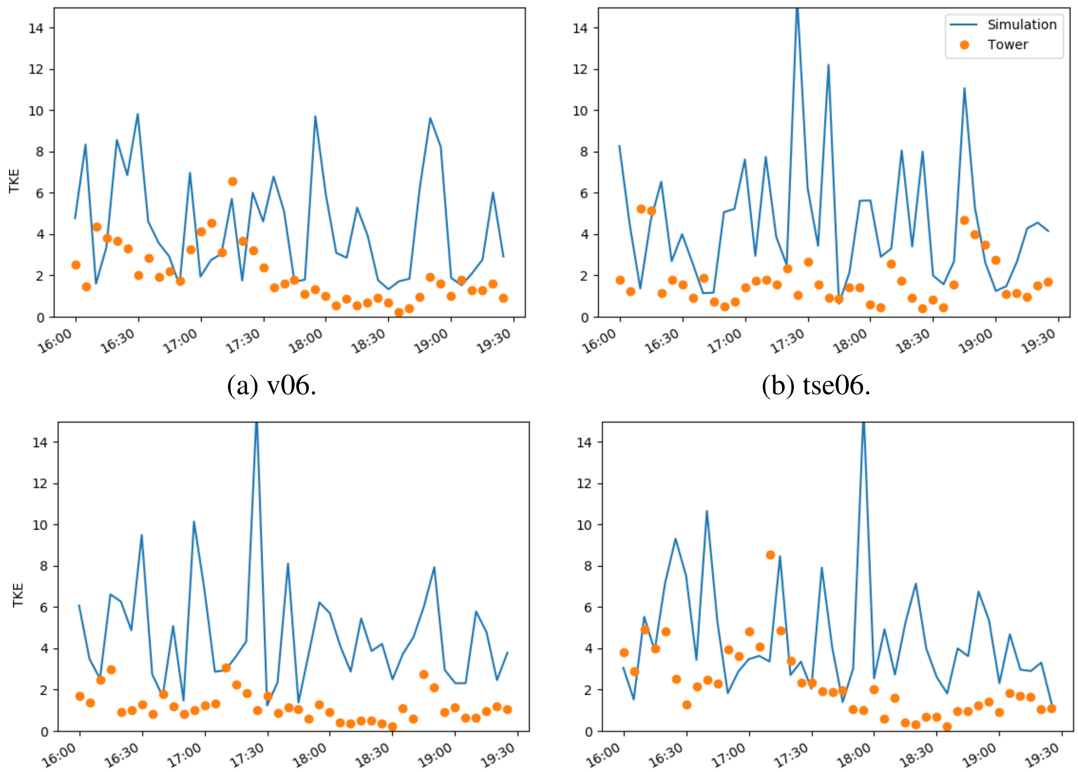

(a) v06.

(b) tse06.

(c) tse07.

(d) tnw07.

Figure 17: TKE comparison between simulated data and tower measurements. Results in (a), (d) and (c) are measured at 20 m AGL and (b) is measured at 60 m AGL.

direction and the TKE of the tower *tnw01* are shown in Figure 18. The results do not show a significant difference, which is expected since CPM only contributes to small scale motions, i.e., the direction of the mean winds and the TKE should not change significantly.

The temporal behaviour for both variables in Figure 18 does change due to the CPM. However, the mean value over time of both variables stays approximately the same. The average wind direction for the simulation without CPM is 228.6 $\pm$ 19.8 degrees and for the simulation with CPM 222.6 $\pm$ 13.6 degrees. The averaged measured wind direction is 229.8 $\pm$ 17.7 degrees and hence CPM does not increase or decrease the accuracy of the simulations accordingly. A similar result is presented in Figure 18(b). The average TKE for the simulation without CPM

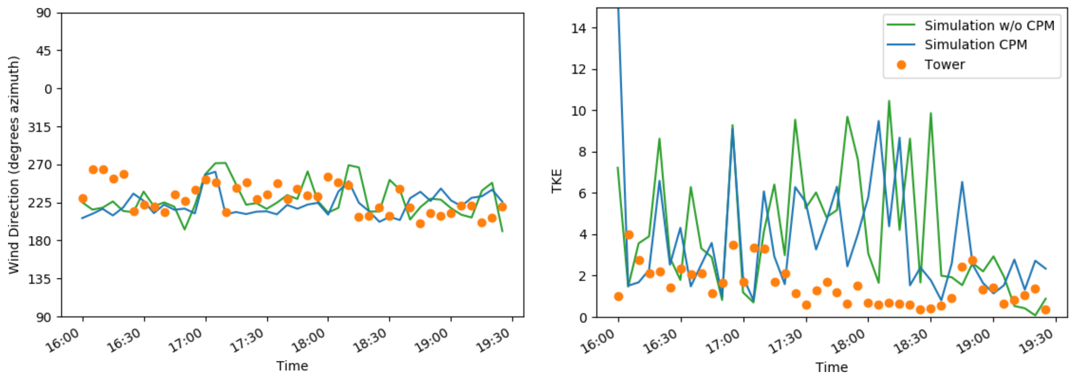

(a) Wind direction ϕ.

(b) Turbulent Kinetic Energy.

Figure 18: Wind direction (a) and TKE (b) comparison at the location of *tnw01* at 20 m AGL between tower measurements and results from two simulations, one with CPM applied on two nested LES domains and one without CPM.

is 4.10 ± 3.02 m^2/s^2 and for the simulation with CPM the average TKE is 3.77 ± 2.96 m^2/s^2, while the average TKE of the tower data is only 1.53 ± 0.93 m^2/s^2. Hence, both simulations are not capable of predicting the correct order of magnitude of the TKE or the prediction of the correct temporal behaviour, as can be seen from Figure 18(b).

5 Conclusions

Nested multiscale modeling is used to represent the evening transition of May 9, 2017 at the Perdigão site in Portugal. The resolutions of the four domains ranged from $\Delta x = 6.75$ km down to $\Delta x = 30$ m. A new coupling strategy, the cell perturbation method (CPM) [Muñoz-Esparza et al., 2014, 2015], is implemented and adapted to the specific situation, particularly paying attention to challenges due to the rough terrain. This is the first time that CPM is applied to a real complex case. To that end the height up to where the perturbations are applied and the height at which the 'weakest' velocity is measured were increased.

The robustness of CPM is demonstrated by comparing the results with CPM to those obtained on a similar but larger domain without CPM. Velocity profiles show that the main structures are unaltered by the method and that only the small scales are enriched. Moreover, spectra comparisons show that these scales are enriched up to a level similar to that of the larger domain, suggesting that CPM successfully accelerates the development of turbulent flow in the nested configuration.

The importance of the precise domain configuration was considered, varying the distance from the location of the interest to the inflow boundary. Only when the spatial domain is sufficiently large the flow can fully develop, implying that the smaller scales contain the correct levels of turbulent kinetic energy. The required size of the spatial domain can be decreased considerably using the cell perturbation method, suggesting savings of at least 25% in the example configurations tested here. The energy spectra are very similar and the main flow structures are unaltered, while the domain size is decreased significantly.

Finally, using a simulation with CPM on two nested LES domains, comparison with actual field data was undertaken. Quite good agreement of the wind direction with tower measurements was found on top of the ridges. The comparisons with tower data from inside the valley show much less good agreement. Moreover, we found that wind speed is significantly over-predicted by the model for all the tower locations, while the turbulent kinetic energy was observed to have about the correct order of magnitude for some of the towers, but showing a very different temporal behaviour. For more sensitive quantities such as wind speed and TKE the model appears to lack qualitative agreement, due to a too coarse resolution and a the lack of a suitable canopy model.

The results from a simulation without CPM showed that the CPM did not significantly increase or decrease the accuracy of the simulation when compared to the field observations. The temporal behaviour of the different variables did change, but the order of magnitude stayed approximately unaltered. A more statistical approach is needed to conclude on a possible improvement using CPM. We expect a better agreement for local variables such as wind speed and TKE for simulations using higher resolution grids and a canopy model. A sensitivity analyses for different mesoscale and LES closure schemes and different forcing systems such as the European Centre for Medium-Range Weather Forecasts (ECMWF) system instead of GFS could possibly suggest an improvement of the model configuration. Finally a sensitivity analysis for the different parameters of CPM, e.g., the height at which the weakest wind speed is approximated and the maximum altitude up to which the perturbations are applied, might show an improvement compared to the settings used in this research.

Acknowledgments

The major part of the research was carried out in the Environmental Fluid Mechanics and Hydrology group at the University of California, Berkeley in close collaboration with James M.T. Neher and supervised by Fotini K. Chow, who both acknowledge support from the National Science Foundation grant AGS-1565483. The author would like to acknowledge high-performance computing support from Cheyenne (doi:10.5065/D6RX99HX) provided by NCAR's Computational and Information Systems Laboratory, sponsored by the National Science Foundation, as well as the Savio computational cluster resource provided by the Berkeley Research Computing program at the University of California, Berkeley (supported by the UC Berkeley Chancellor, Vice Chancellor for Research, and Chief Information Officer). The author expresses great appreciation for the members of the Environmental Fluid Mechanics and Hydrology group and the researchers participating in the Perdigão Field Campaign for their support and additionally to Jeff Mirocha for his help with implementing the CPM code. Finally the author would like to thank James M.T. Neher and both of his supervisors, Fotini K. Chow and Bernard J. Geurts for their help and supervision regarding this research in general.

References

F. K. Chow and R. L. Street. Evaluation of turbulence closure models for Large-Eddy simulation over complex terrain: Flow over Askervein Hill. *Journal of Applied Meteorology and Climatology*, 48(5):1050–1065, 2009. doi: 10.1175/2008JAMC1862.1.

M. H. Daniels, K. A. Lundquist, J. D. Mirocha, D. J. Wiersema, and F. K. Chow. A New Vertical Grid Nesting Capability in the Weather Research and Forecasting (WRF) Model. *Monthly Weather Review*, 144(10):3725–3747, 2016. doi: 10.1175/MWR-D-16-0049.1.

D. Durran, J. A. Weyn, and M. Q. Menchaca. Practical Considerations for Computing Dimensional Spectra from Gridded Data. *Monthly Weather Review*, 145(9):3901–3910, 2017. ISSN 0027-0644. doi: 10.1175/MWR-D-17-0056.1.

M. Jähn, D. Muñoz-Esparza, F. Chouza, O. Reitebuch, O. Knoth, M. Haarig, and A. Ansmann. Investigations of boundary layer structure, cloud characteristics and vertical mixing of aerosols at Barbados with large eddy simulations. *Atmospheric Chemistry and Physics*, 16 (2):651–674, 2016. doi: 10.5194/acp-16-651-2016.

P. A. Jiménez and J. Dudhia. Improving the representation of resolved and unresolved topographic effects on surface wind in the wrf model. *Journal of Applied Meteorology and Climatology*, 51(2):300–316, 2 2012. doi: 10.1175/JAMC-D-11-084.1.

S. Lardeau, N. Li, and M. A. Leschziner. Large Eddy Simulation of Transitional Boundary Layers at High Free-Stream Turbulence Intensity and Implications for RANS Modeling. *Journal of Turbomachinery*, 129(2):311, 4 2007. doi: 10.1115/1.2436896.

D. K. Lilly. The Representation of Small-Scale Turbulence in Numerical Simulation Experiments. *Proceedings of the IBM Scientific Computing Symposium on Environmental Sciences*, no. 281(November):195–210, 1967. doi: 10.5065/D62R3PMM.

T. S. Lund, X. Wu, and K. D. Squires. Generation of Turbulent Inflow Data for Spatially-

Developing Boundary Layer Simulations. *Journal of Computational Physics*, 140(2):233–258, 3 1998. doi: 10.1006/jcph.1998.5882.

L. J. Mazzaro, D. Muñoz-Esparza, J. K. Lundquist, and R. R. Linn. Nested mesoscale-to-LES modeling of the atmospheric boundary layer in the presence of under-resolved convective structures. *Journal of Advances in Modeling Earth Systems*, 2017. doi: 10.1002/2017MS000912.

J. D. Mirocha, B. Kosović, and G. Kirkil. Resolved Turbulence Characteristics in Large-Eddy Simulations Nested within Mesoscale Simulations Using the Weather Research and Forecasting Model. *Monthly Weather Review*, 142(2):806–831, 2014. doi: 10.1175/MWR-D-13-00064.1.

D. Muñoz-Esparza, B. Kosović, J. D. Mirocha, and J. van Beeck. Bridging the Transition from Mesoscale to Microscale Turbulence in Numerical Weather Prediction Models. *Boundary-Layer Meteorology*, 153(3):409–440, 2014. doi: 10.1007/s10546-014-9956-9.

D. Muñoz-Esparza, B. Kosović, J. V. Beeck, and J. D. Mirocha. A stochastic perturbation method to generate inflow turbulence in large-eddy simulation models Application to neutrally stratified atmospheric boundary layers A stochastic perturbation method to generate inflow turbulence in large-eddy simulation models. *Physics of Fluids*, 035102(035102):1–43, 2015. doi: 10.1063/1.4913572.

D. Muñoz-Esparza, J. K. Lundquist, J. A. Sauer, B. Kosović, and R. R. Linn. Coupled mesoscale-LES modeling of a diurnal cycle during the CWEX-13 field campaign: From weather to boundary-layer eddies. *Journal of Advances in Modeling Earth Systems*, 9(3):1572–1594, 2017. doi: 10.1002/2017MS000960.

M. Nakanishi and H. Niino. An improved Mellor-Yamada Level-3 model with condensation physics: Its design and verification. *Boundary-Layer Meteorology*, 112(1):1–31, 2004. doi: 10.1023/B:BOUN.0000020164.04146.98.

H. Nakayama, T. Takemi, and H. Nagai. Large-eddy simulation of urban boundary-layer flows by generating turbulent inflows from mesoscale meteorological simulations. *Atmospheric Science Letters*, 13(3):180–186, 2012. doi: 10.1002/asl.377.

F. Ngan, H. Kim, P. Lee, K. Al-Wali, and B. Dornblaser. A study of nocturnal surface wind speed overprediction by the WRF-ARW model in Southeastern Texas. *Journal of Applied Meteorology and Climatology*, 52(12):2638–2653, 12 2013. doi: 10.1175/JAMC-D-13-060.1.

R. K. Rai, L. K. Berg, B. Kosović, J. D. Mirocha, M. S. Pekour, and W. J. Shaw. Comparison of Measured and Numerically Simulated Turbulence Statistics in a Convective Boundary Layer Over Complex Terrain. *Boundary-Layer Meteorology*, 163(1):69–89, 2017. doi: 10.1007/s10546-016-0217-y.

W. C. Skamarock. Evaluating Mesoscale NWP Models Using Kinetic Energy Spectra. *Monthly Weather Review*, 132(12):3019–3032, 2004. doi: 10.1175/MWR2830.1.

W. C. Skamarock and J. B. Klemp. A time-split nonhydrostatic atmospheric model for weather research and forecasting applications. *Journal of Computational Physics*, 227(7):3465–3485, 3 2008. doi: 10.1016/j.jcp.2007.01.037.

J. C. Wyngaard. Toward Numerical Modeling in the Terra Incognita. *Journal of the Atmospheric Sciences*, 61(14):1816–1826, 2004. doi: 10.1175/1520-0469(2004)061⟨1816:TNMITT⟩2.0.CO;2.

B. Zhou and F. K. Chow. Nested Large-Eddy Simulations of the Intermittently Turbulent Stable Atmospheric Boundary Layer over Real Terrain. *Journal of the Atmospheric Sciences*, 71(3):1021–1039, 2014. doi: 10.1175/JAS-D-13-0168.1.

B. Zhou, J. S. Simon, and F. K. Chow. The Convective Boundary Layer in the Terra Incognita. *Journal of the Atmospheric Sciences*, 71(7):2545–2563, 2014. doi: 10.1175/JAS-D-13-0356.1.